Advanced Energy Conversion Materials
http://ojs.wiserpub.com/index.php/AECM/

UNIVERSAL WISER PUBLISHER

Research Article

Physical Properties of SnO_2/WO_3 Bilayers Prepared by Reactive DC Sputtering

C. Guillén

Research Centre for Energy, Environment and Technology, Complutense Avenue 40, 28040 Madrid, Spain
E-mail: c.guillen@ciemat.es

Received: 29 April 2023; **Revised:** 7 June 2023; **Accepted:** 8 June 2023

Abstract: The combination of transparent and conductive SnO_2 with colored WO_3 thin films has interesting uses in electrochromic windows, photovoltaic cells and photocatalytic systems, where the SnO_2/WO_3 bilayer can improve the device efficiency by increasing the charge separation and extending the energy range of photoexcitation. In this work, SnO_2 and WO_3 thin films were prepared by reactive DC sputtering from Sn and W targets, respectively. Single layers and bilayers deposited on glass substrates have been analyzed by X-ray diffraction, atomic force microscopy, spectrophotometry, and electrical measurements. SnO_2 crystallizes in the cassiterite structure, whereas amorphous WO_3 is obtained on bare and SnO_2-coated glasses, showing higher surface roughness on the SnO_2 layer. Different oxygen vacancy defects have been identified in WO_3 by analyzing photoconductivity transients. The oxygen vacancy defects are responsible for the sub-bandgap absorption that causes coloration in the WO_3 films. Regarding SnO_2, it shows a high transmittance of about 90% in the visible and near-infrared spectral ranges.

***Keywords*:** metal oxides, sputtering, thin films, electrical conductivity, optical transmittance

1. Introduction

Metal oxide thin films are being developed for multiple applications, from electronics to energy harvesting and hydrogen storage, including flat panel displays, photovoltaic cells, electrochromic windows, and thin-film transistors [1, 2]. Two types of oxide materials are mainly used for these thin-film devices: Transition Metal Oxides (TMO) [2] and Transparent Conductive Oxides (TCO) [1]. SnO_2 belongs to the TCO group, with high transparency in the visible region owing to its wide bandgap energy (about 3.6 eV), and intrinsic n-type conductivity due to a low formation energy for donor defects (tin interstitials and oxygen vacancies) [3]. Besides, WO_3 is a typical TMO with an empty W 5d derived conduction band, and a valence band constituted by O 2p hybridized with filled W 5d orbitals [2]. The band-to-band transition is about 3.0 eV, but oxygen vacancy defects introduce additional electronic states in the bands, leading to chromogenic properties [4]. More specifically, SnO_2/WO_3 bilayers are used in electrochromic windows [5], photovoltaic devices [6], gas sensors [7] and photocatalytic applications [8], where the coupled semiconductor system has shown high efficiency in increasing the charge separation and extending the energy range of photoexcitation. Although the effect of SnO_2/WO_3 bilayers on the performance of various devices has been proven, a detailed study of the physical properties of the bilayer itself in comparison with the constituent layers is lacking. The main issue addressed here is to

DOI: https://doi.org/10.37256/aecm.4220232941

determine the properties of the bilayers as a function of the preparation conditions.

Among the various deposition methods that have been used to prepare SnO_2/WO_3 bilayers, the sputtering technique stands out, either in the Radio Frequency (RF) mode with ceramic targets [6] or in the reactive Direct Current (DC) mode with metallic targets [7]. The sputtering technique is suitable for the large-scale fabrication of cost-effective metal oxide films, allowing a high degree of controllability of the oxygen vacancy defects [4]. Reactive DC sputtering is especially attractive due to the low cost of metal targets and easy control of film stoichiometry via oxygen gas flow [9, 10].

In the present work, SnO_2/WO_3 bilayers have been prepared by reactive DC sputtering from Sn and W targets, adjusting the flow of oxygen gas to obtain high transparency and conductivity for SnO_2 and visible light absorption for WO_3. The structure, morphology, optical and electrical properties have been analyzed for each individual layer and for the stack deposited on glass substrates. The goal is to gain a better understanding of the interrelationship between the different features and their modification by deposition conditions, which can contribute to the further expansion of SnO_2/WO_3 bilayers for multiple applications.

2. Experimental procedure

2.1 *Synthesis*

Thin films were deposited by reactive DC magnetron sputtering on unheated Soda-Lime Glasses (SLG). The targets were discs of 15 cm diameter, provided by Mateck under request for Sn (purity 99.99%) and W (purity 99.99%). After the evacuation of the deposition chamber to a base pressure of 4×10^{-4} Pa, oxygen and argon gases were introduced by independent mass flow controllers. SnO_2 layers were deposited with a discharge power of 200 W and an oxygen partial pressure $O_{pp} = p(O_2)/(p(Ar) + p(O_2)) = 0.24$, giving a growth rate of 50 nm/min, as has been reported in a previous paper [11]. WO_3 films were prepared with a discharge power of 200 W and an oxygen ratio $O_{pp} = 0.12$ or $O_{pp} = 0.10$, at a growth rate of 25 nm/min, according to previous works [12, 13]. For each case, the deposition time was adjusted to obtain the same film thickness of about 0.4 μm.

2.2 *Characterization*

The crystallographic properties were examined by X-Ray Diffraction (XRD) with radiation Cu K-α1 (λ = 1.54056 Å) in a Philips X'pert instrument, using Bragg-Brentano θ-2θ configuration. The standard Powder Diffraction Files (PDF) were consulted to identify the crystalline phases in the diffractograms. The mean crystallite size was calculated from the full width at half maximum of the diffraction peak, applying the Scherrer formula [14]. The atomic composition was measured with a Fischer X-ray fluorescence analyzer using a tungsten anode. The topography was inspected by Atomic Force Microscopy (AFM) with a Park XE-100 system, which allows for quantifying surface roughness from digital images.

Electrical measurements were made with a Keithley 2635A nanoammeter and a Keithley 2420 voltage source. Photosensitivity was determined using a 50 W halogen lamp placed 7 cm above the sample, which was turned on and off successively during I-V data acquisition. In addition, sheet resistance was obtained using a four-point probe system Veeco FPP5000. The optical characterization was based on transmittance (T) and reflectance (R) measurements done with a double beam spectrophotometer Perkin-Elmer Lambda 9 at wavelengths from 250 to 2,500 nm, taking the air as a reference. The absorption coefficient has been calculated by the expression $\alpha = (1/t)\ \ln\{(100 - R(\%))/T(\%)\}$ [15], including the film thickness value (t) measured with a Dektak 3030 profilometer.

3. Results and discussion

The most relevant characteristics of the samples are summarized in Table 1. These WO_3 films are amorphous, as deduced from the absence of diffraction peaks in the XRD patterns. On the other hand, the SnO_2 exhibits diffraction peaks from the (110), (101), (200) and (211) planes according to the tetragonal cassiterite structure (PDF 41-1445). They are shown in Figure 1 for the isolated film and in the bilayer with WO_3-A (deposited at $O_{pp} = 0.12$) or WO_3-B

(deposited at O_{pp} = 0.10). The peak intensities are in accordance with the SnO_2 powder standard, I(110)/I(200) ~ 4.9 and I(110)/I(211) ~ 1.7, except I(101) which is higher than expected from the standard ratio: I(101)/I(110) > 0.7. An increase in (101) orientation has been observed for other polycrystalline SnO_2 films prepared by reactive sputtering at relatively low oxygen pressures [16, 17]. This is explained because in reducing environments (poor in oxygen) the (101) surface is more stable than the (110) surface [17]. The mean crystallite sizes obtained for SLG/SnO_2 (S_{110} = 5 nm, S_{101} = 8 nm, S_{211} = 8 nm), SLG/SnO_2/WO_3-A (S_{110} = 4 nm, S_{101} = 7 nm, S_{211} = 7 nm) and SLG/SnO_2/WO_3-B (S_{110} = 4 nm, S_{101} = 7 nm, S_{211} = 7 nm) are the same with an experimental error of ± 1 nm. They are within the range reported for analogous tin oxide films prepared by reactive sputtering [16], for which limited crystallite growth is related to the abundance of intrinsic defects, such as oxygen vacancies and/or tin interstitials.

Table 1. Summary of the most relevant characteristics of the samples, including the oxygen partial pressure during sputtering (O_{pp}), film thickness (t), oxygen to the metal atomic ratio (O/Me), root-mean-square roughness (r), sheet resistance (R_s), average transmittance in the visible and near-infrared (T_{vis}, T_{ir}), and optical bandgap (E_g)

Sample	O_{pp}	t (μm)	O/Me (at %)	r (nm)	R_s (Ω/sq)	T_{vis} (%)	T_{ir} (%)	E_g (eV)
SnO_2	0.24	0.46	1.95	0.6	102	91	89	3.42
WO_3-A	0.12	0.38	2.95	0.3	8×10^5	58	48	3.34
WO_3-B	0.10	0.40	2.85	0.4	6×10^4	17	30	3.08
SnO_2/WO_3-A	-	0.84	-	1.1	102	62	48	3.35
SnO_2/WO_3-B	-	0.86	-	1.1	102	16	24	3.12

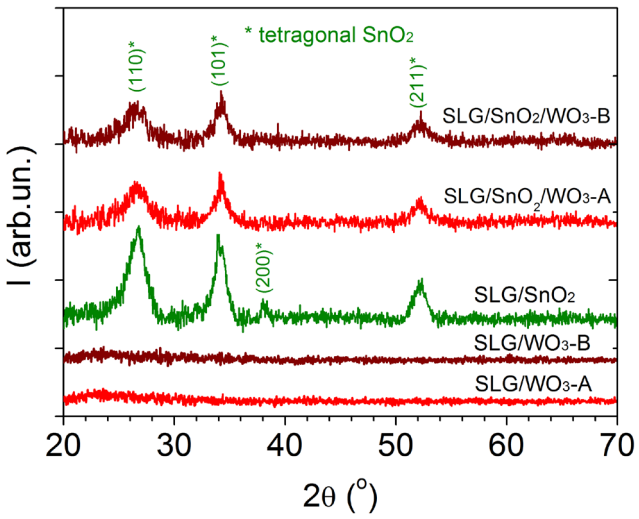

Figure 1. XRD patterns corresponding to the individual films and SnO_2/WO_3 bilayers prepared on soda-lime glasses

The surface morphology of the different samples and the corresponding root-mean-square roughness (r) is illustrated in Figure 2. Individual films show smooth surfaces with a lower roughness value for amorphous WO_3 (r = 0.3-0.4 nm) than for polycrystalline SnO_2 (r = 0.6 nm). Flat surfaces, with r < 1 nm, have been found for similar WO_3 and SnO_2 films sputtered on glass substrates, with a slight increase in roughness as oxygen content decreases [9, 18]. The SnO_2/WO_3 stacks exhibit a rougher surface (r = 1.1 nm), as has been observed for evaporated bilayers in

comparison with the individual evaporated films [8]. This is attributed to compressive/tensile stresses at the interface of the bilayers [19], which are not important because cracks or adhesion failures have not been detected in any case. An increase in the effective surface of the SnO_2/WO_3 bilayer can be useful for several applications, such as photocatalytic devices and gas sensors [8, 20].

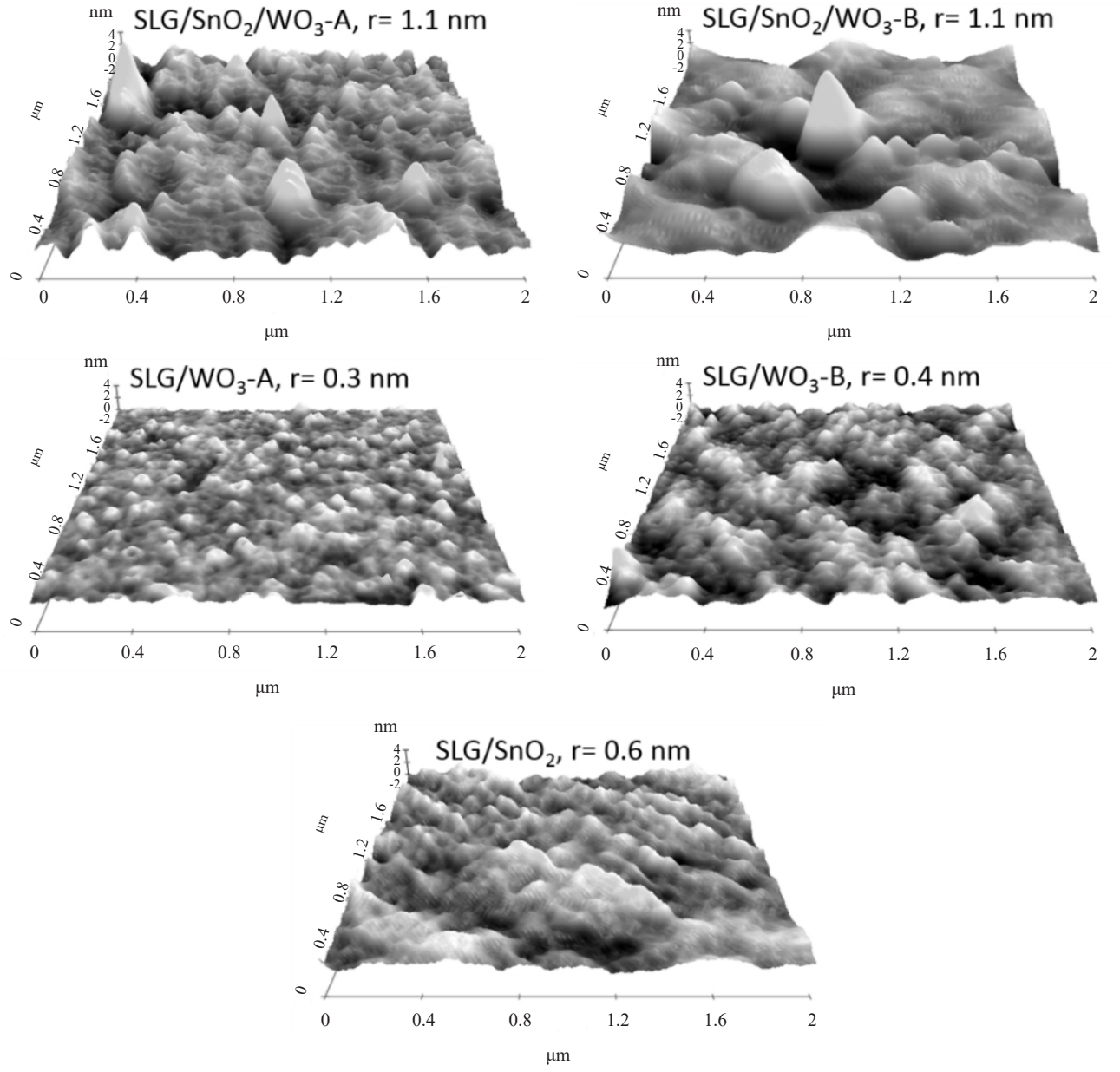

Figure 2. AFM images taken on 2 µm × 2 µm areas for the individual films and SnO_2/WO_3 bilayers. The root-mean-square roughness (r) value for each sample is included

The sheet resistance and thickness data in Table 1 show that the electrical conductivity, $\sigma = (R_s t)^{-1}$, is much higher for SnO_2 (10^2 S/cm) than for WO_3-A (10^{-2} S/cm) and WO_3-B (10^{-1} S/cm). For the SnO_2/WO_3 samples, the total resistance agrees with a parallel connection of the respective resistances: $R_{bilayer} = (1/R_{SnO_2} + 1/ R_{WO_3})^{-1} \approx R_{SnO_2}$, with a clear predominance of the most conductive material as reported for other bilayers [21]. Regarding photosensitivity, the

SnO_2 layer and the SnO_2/WO_3 bilayers have not presented appreciable changes in conductivity under dark and light conditions. This is common in highly conductive materials where the concentration of photogenerated carriers is several orders of magnitude lower than that of free carriers in the dark. Comparing the individual WO_3 films, Figure 3 shows that the photoresponse is higher for WO_3-A (with $\Delta\sigma_{light}/\sigma_{dark} = 5.4 \times 10^{-2}$) than for WO_3-B (with $\Delta\sigma_{light}/\sigma_{dark} = 1.5 \times 10^{-3}$). The contribution of photogenerated carriers is less important in WO_3-B, which has a higher conductivity in the dark due to a higher proportion of donor oxygen vacancies. On the other hand, the lower conductivity of WO_3-A slowly increases under illumination and also slowly decays when the light is turned off. This is due to traps related to intrinsic defects [22], which have been investigated according to the rise and decay equations [23, 24]:

$$\sigma_{rise} = \sigma_{dark} + \Delta\sigma_{light}\left(1 - \Sigma_i\, A_i\, exp\left\{-t_{on} / \tau_{r,i}\right\}\right) \quad (1)$$

$$\sigma_{decay} = \sigma_{dark} + \Delta\sigma_{light}\left(\Sigma_i\, A_i\, exp\left\{-t_{off} / \tau_{d,i}\right\}\right) \quad (2)$$

where σ_{dark} is the conductivity in dark, $\Delta\sigma_{light}$ is the steady-state photoconductivity, t_{on} is the time with the light on, t_{off} the time after illumination turned off, A_i is a proportionality factor ($\Sigma_i A_i = 1$) and t_i the time constant for the different trap levels acting in the photoconductivity transients. The time constant is related to the trapped energy by the equation [25]:

$$\tau = (1/v)\, exp(E_t / kT) \quad (3)$$

where E_t is the trap energy, kT the thermal energy (25.68 meV) and v is the lattice vibration frequency (10^{13} s^{-1}) [26].

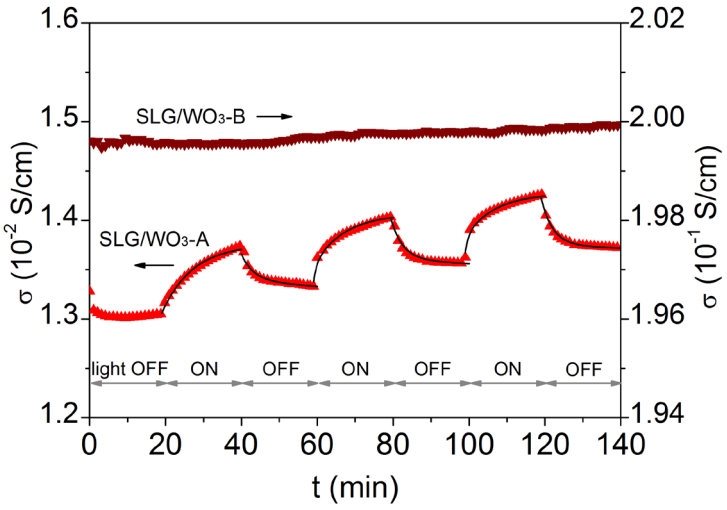

Figure 3. Electrical conductivity of the films grown under different oxygen pressures (WO_3-A at $O_{pp} = 0.12$ and WO_3-B at $O_{pp} = 0.10$) as a function of time under dark or light conditions

The experimental data fit for SLG/WO_3-A in Figure 3 give three levels with time constants $t_1 = 114$ s, $t_2 = 480$ s and $t_3 = 4{,}830$ s; corresponding to trap energies $E_{t1} = 0.89$ eV, $E_{t2} = 0.93$ eV and $E_{t3} = 0.99$ eV. Different models for the electronic structure of oxygen-deficient WO_3 predict the occurrence of various defect states in the range 0-1 eV below the conduction band, which are due to oxygen vacancies (V_O) at different charge states [27, 28]. The obtained E_t values are in agreement with the transition levels V_O^{+}/V_O^{0}, V_O^{++}/V_O^{+} and V_O^{++}/V_O^{0}, located at increasing energies from the conduction band [27, 29].

The optical transmittance and reflectance of the individual and stacked layers are plotted in Figure 4 as a function

of the light wavelength, including data for the bare SLG substrate. SnO_2 shows high transmittance in both the visible (λ = 400-800 nm) and near-infrared (λ = 800-2,500 nm) ranges, with $T_{vis} = T_{ir} = 90 \pm 1\%$ taking as reference the bare Soda Lime Glass (SLG) substrate. Lower transmittances are obtained for WO_3-A ($T_{vis} = 60 \pm 2\%$, $T_{ir} = 48 \pm 1\%$) and WO_3-B ($T_{vis} = 17 \pm 1\%$, $T_{ir} = 27 \pm 3\%$) as detailed in Table 1. The decrease in transmittance in WO_3 is related to an increase of oxygen vacancy defects (V_O^+ and/or V_O^{++}) bound to tungsten atoms in a lower oxidation state (W^{5+} and/or W^{4+}), which cause sub-bandgap absorption [30]. Therefore, the lower optical transmittance values confirm that the proportion of oxygen vacancies is higher for WO_3 grown at lower O_{pp}.

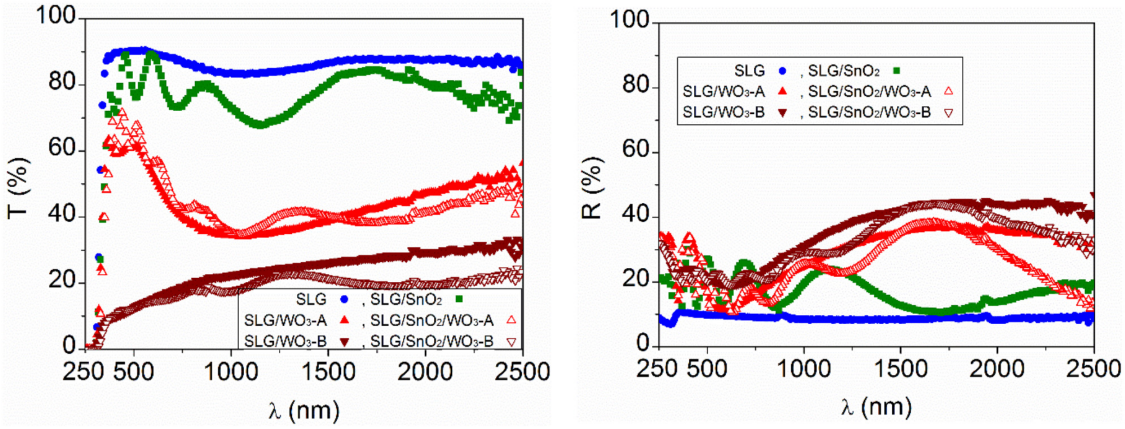

Figure 4. Optical transmittance and reflectance measured for the various samples as a function of the light wavelength. Data for the bare SLG substrate are added for comparison

The corresponding optical absorption coefficients (α) are plotted in Figure 5 as a function of the light Energy (E). The absorption growth in the high energy region (E > 3.3 eV) is due to interband transitions over the semiconductor bandgap, showing a good fit to the relationship $\alpha_i = (A/E) \cdot (E - E_g)^2$, which is typical of indirect transitions. The bandgap energy is obtained from the plot of $(\alpha E)^{1/2}$ vs. E, by prolonging the linear part of the curve to the E axis. The calculated value is $E_g = 3.42$ eV for SnO_2, $E_g = 3.35 \pm 0.01$ eV for WO_3-A and $E_g = 3.10 \pm 0.02$ eV for WO_3-B. These bandgap energies (included in Table 1) are in agreement with those reported for analogous thin films of SnO_2 [31] and WO_3 [12, 32].

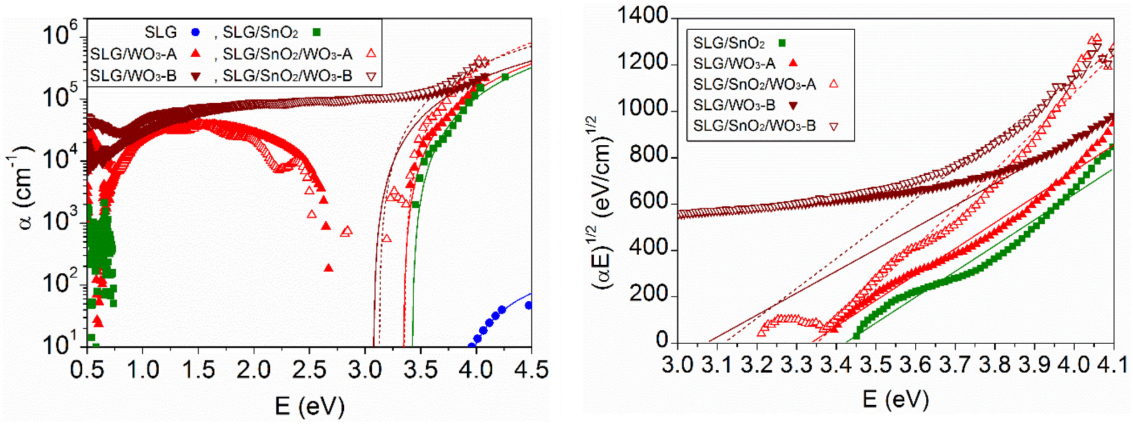

Figure 5. Optical absorption coefficient obtained for the different samples as a function of light energy, including bare SLG substrate data. The lines represent the absorption due to the indirect bandgap transition

Furthermore, the WO_3 layers show a pronounced absorption below the bandgap energy, related to oxygen deficiency [30]. The sub-stoichiometric compound is considered a mixture of W^{6+} with W^{5+} and W^{4+} states, sub-bandgap absorption increasing by around 1.5 eV with the W^{5+} content and above 3 eV with the W^{4+} ratio [12]. For SnO_2, some sub-bandgap absorption is also detected at energies below 0.8 eV. This is due to the absorption of near-infrared radiation by free electrons, typical of conductive metal oxides [33, 34], which has been analyzed for analogous sputtered SnO_2 films in previous work [35].

4. Conclusions

SnO_2/WO_3 bilayers were prepared by reactive DC sputtering on glass substrates. Their structure, morphology, an optical and electrical properties were analyzed in comparison with the individual films. According to X-ray diffraction, the addition of WO_3 onto SnO_2 does not lead to the appearance of crystalline phases other than tetragonal SnO_2 one, which has a mean crystallite size of 4 nm in the (110) orientation and 8 nm in the (101) and (211) orientations. The WO_3 layers are amorphous on the bare and SnO_2-coated glasses, showing a higher surface roughness on the SnO_2 film (r = 1.1 nm) than on the uncoated glass (r = 0.3-0.4 nm). The increase in roughness is attributed to some stress at the interface of the bilayer, which is low enough to keep the samples well-adhered and free of cracks.

The total resistance of the SnO_2/WO_3 bilayers is consistent with a parallel connection of the two materials, being in fact the same as that of SnO_2 due to its high conductivity (10^2 S/cm) compared to WO_3 (10^{-1} – 10^{-2} S/cm). On the other hand, the optical transmittance of the bilayers is dominated by WO_3, which reaches high absorption coefficients in the visible and near-infrared. This optical absorption is due to the presence of sub-stoichiometric states W^{5+} and W^{4+}, which can be increased by decreasing the oxygen partial pressure during WO_3 deposition.

These SnO_2/WO_3 bilayers show improved characteristics respecting the individual films, with an overall transmittance analogous to the WO_3 layer and electrical conductivity as SnO_2. They are prepared by a scalable method, which facilitates their application in electrochromic windows and other electro-optical devices that require good electrical conductivity and light absorption in the visible and near-infrared.

Conflict of interest

The author declares that there is no conflict of interest. They have no known competing financial interests or personal relationships that could have appeared to influence the work reported in this paper.

References

[1] Nathan A, Jeon S. Oxide electronics: Translating materials science from lab-to-fab. *MRS Bulletin*. 2021; 46: 1028-1036. Available from: doi: 10.1557/s43577-021-00257-3.

[2] Li W, Shi J, Zhang KHL, MacManus-Driscoll JL. Defects in complex oxide thin films for electronics and energy applications: challenges and opportunities. *Materials Horizons*. 2020; 7: 2832-2859. Available from: doi: 10.1039/D0MH00899K.

[3] Kíliç C, Zunger A. Origins of coexistence of conductivity and transparency in SnO_2. *Physical Review Letters*. 2002; 88: 95501. Available from: doi: 10.1103/PhysRevLett.88.095501.

[4] Thummavichai K, Xia Y, Zhu Y. Recent progress in chromogenic research of tungsten oxides towards energy-related applications. *Progress in Materials Science*. 2017; 88: 281-324. Available from: doi: 10.1016/j.pmatsci.2017.04.003.

[5] Wei W, Li Z, Guo Z, Li Y, Hou F, Guo W, et al. An electrochromic window based on hierarchical amorphous WO_3/SnO_2 nanoflake arrays with boosted NIR modulation. *Applied Surface Science*. 2022; 571: 151277. Available from: doi: 10.1016/j.apsusc.2021.151277.

[6] Otoufi MK, Ranjbar M, Kermanpur A, Taghavinia N, Heydari M. Synthesis and optimization of planar perovskite solar cells using TiO_2/SnO_2, TiO_2/WO_3 and SnO_2/WO_3 electron transport bilayer structures. *Journal of Advanced Materials and Technologies*. 2021; 10: 1-12. Available from: doi: 10.30501/jamt.2021.225445.1084.

[7] Toan N Van, Hung CM, Duy N Van, Hoa ND, Le DTT, Hieu N Van. Bilayer SnO_2-WO_3 nanofilms for enhanced NH_3 gas sensing performance. *Materials Science and Engineering: B*. 2017; 224: 163-170. Available from: doi: 10.1016/j.mseb.2017.08.004.
[8] Arfaoui A, Mhamdi A, Besrour N, Touihri S, Ouzari HI, Alrowaili ZA, et al. Investigations into the physical properties of SnO_2/MoO_3 and SnO_2/WO_3 bi-layered structures along with photocatalytic and antibacterial applications. *Thin Solid Films*. 2018; 648: 12-20. Available from: doi: 10.1016/j.tsf.2018.01.002.
[9] Tao Y, Zhu B, Yang Y, Wu J, Shi X. The structural, electrical, and optical properties of SnO_2 films prepared by reactive magnetron sputtering: Influence of substrate temperature and O_2 flow rate. *Materials Chemistry and Physics*. 2020; 250: 123129. Available from: doi: 10.1016/j.matchemphys.2020.123129.
[10] Joël-Igor N'Djoré KB, Grafouté M, Bulou A, Rousselot C. Correlation between physical properties and electrochromic performances of DC magnetron sputtered a-WO_x thin films. *Materials Science and Engineering: B*. 2023; 290: 116261. Available from: doi: 10.1016/j.mseb.2023.116261.
[11] Guillén C, Herrero J. Intrinsic and extrinsic doping contributions in SnO_2 and SnO_2:Sb thin films prepared by reactive sputtering. *Journal of Alloys and Compounds*. 2019; 791: 68-74. Available from: doi: 10.1016/j.jallcom.2019.03.302.
[12] Guillén C, Herrero J. Amorphous WO_{3-x} thin films with color characteristics tuned by the oxygen vacancies created during reactive DC sputtering. *Journal of Materials Science & Technology*. 2021; 78: 223-228. Available from: doi: 10.1016/j.jmst.2020.11.036.
[13] Guillén C. Polycrystalline WO_{3-x} thin films obtained by reactive DC sputtering at room temperature. *Materials (Basel)*. 2023; 16: 1359. Available from: doi: 10.3390/ma16041359.
[14] Vorokh AS. Scherrer formula: estimation of error in determining small nanoparticle size. *Nanosystems: Physics, Chemistry, Mathematics*. 2018; 9: 364-369. Available from: doi: 10.17586/2220-8054-2018-9-3-364-369.
[15] Demichelis F, Kaniadakis G, Tagliaferro A, Tresso E. New approach to optical analysis of absorbing thin solid films. *Applied Optics*. 1987; 26: 1737-1740. Available from: doi: 10.1364/AO.26.001737.
[16] Bansal S, Pandya DK, Kashyap SC, Haranath D. Growth ambient dependence of defects, structural disorder and photoluminescence in SnO_2 films deposited by reactive magnetron sputtering. *Journal of Alloys and Compounds*. 2014; 583: 186-190. Available from: doi: 10.1016/j.jallcom.2013.08.135.
[17] Körber C, Suffner J, Klein A. Surface energy controlled preferential orientation of thin films. *Journal of Physics D: Applied Physics*. 2010; 43: 55301. Available from: doi: 10.1088/0022-3727/43/5/055301.
[18] Lu HH. Effects of oxygen contents on the electrochromic properties of tungsten oxide films prepared by reactive magnetron sputtering. *Journal of Alloys and Compounds*. 2008; 465: 429-435. Available from: doi: 10.1016/j.jallcom.2007.10.105.
[19] Murugesan M, Arjunraj D, Mayandi J, Venkatachalapathy V, Pearce JM. Properties of Al-doped zinc oxide and In-doped zinc oxide bilayer transparent conducting oxides for solar cell applications. *Materials Letters*. 2018; 222: 50-53. Available from: doi: 10.1016/j.matlet.2018.03.097.
[20] Dong C, Zhao R, Yao L, Ran Y, Zhang X, Wang Y. A review on WO_3 based gas sensors: Morphology control and enhanced sensing properties. *Journal of Alloys and Compounds*. 2020; 820: 153194. Available from: doi: 10.1016/j.jallcom.2019.153194.
[21] Doghmane NEA, Chettibi S, Challali F, Chelouche A, Touam T. Confocal magnetron sputtering deposition of Cu/AZO bilayer structures: effect of Cu thickness on microstructural and optoelectronic properties. *Journal of Materials Science: Materials in Electronics*. 2022; 33: 26717-26727. Available from: doi: 10.1007/s10854-022-09338-8.
[22] Chandan, Sarkar S, Angadi B. Defects induced persistent photoconductivity in monolayer MoS_2. *Applied Physics Letters*. 2021; 118: 172105. Available from: doi: 10.1063/5.0048505.
[23] Sharma A, Bhattacharyya B, Srivastava AK, Senguttuvan TD, Husale S. High performance broadband photodetector using fabricated nanowires of bismuth selenide. *Scientific Reports*. 2016; 6: 19138. Available from: doi: 10.1038/srep19138.
[24] Traoré A, Gouveia M, Okumura H, Mannequin C, Fassion A, Sakurai T. Photo-induced conductivity transient in n-type β-$(Al_{0.16}Ga_{0.84})_2O_3$ and β-Ga_2O_3. *Japanese Journal of Applied Physics*. 2021; 60: SBBD15. Available from: doi: 10.35848/1347-4065/abe5bd.
[25] Studenikin SA, Golego N, Cocivera M. Density of band-gap traps in polycrystalline films from photoconductivity transients using an improved laplace transform method. *Journal of Applied Physics*. 1998; 84: 5001. Available from: doi: 10.1063/1.368746.
[26] Hao J, Studenikin SA, Cocivera M. Transient photoconductivity properties of tungsten oxide thin films prepared by

spray pyrolysis. *Journal of Applied Physics*. 2001; 90: 5064-5069. Available from: doi: 10.1063/1.1412567.
[27] Gerosa M, Di Valentin C, Onida G, Bottani CE, Pacchioni G. Anisotropic effects of oxygen vacancies on electrochromic properties and conductivity of γ-monoclinic WO_3. *The Journal of Physical Chemistry C*. 2016; 120: 11716-11726. Available from: doi: 10.1021/acs.jpcc.6b02707.
[28] De Wijs GA, De Groot RA. Structure and electronic properties of amorphous WO_3. *Physical Review B*. 1999; 60: 16463-16474. Available from: doi: 10.1103/PhysRevB.60.16463.
[29] Wang B, Zhong X, Xu H, Zhang Y, Cvelbar U, Ostrikov K. Structure and photoluminescence of WO_{3-x} aggregates tuned by surfactants. *Micromachines*. 2022; 13: 2075. Available from: doi: 10.3390/mi13122075.
[30] Berggren L, Niklasson GA. Optical absorption and durability of sputtered amorphous tungsten oxide films. *Solid State Ionics*. 2003; 165: 51-58. Available from: doi: 10.1016/j.ssi.2003.08.016.
[31] Giulio M Di, Manno D, Micocci G, Rella R, Siciliano P, Tepore A. Growth and characterization of tin oxide thin films prepared by reactive sputtering. *Solar Energy Materials and Solar Cells*. 1993; 31: 235-242. Available from: doi: 10.1016/0927-0248(93)90054-7.
[32] Demiryont H, Nietering KE. Tungsten oxide films by reactive and conventional evaporation techniques. *Applied Optics*. 1989; 28: 1494. Available from: doi: 10.1364/AO.28.001494.
[33] Deyu GK, Muñoz-Rojas D, Rapenne L, Deschanvres JL, Klein A, Jiménez C, et al. SnO_2 films deposited by ultrasonic spray pyrolysis: Influence of Al incorporation on the properties. *Molecules*. 2019; 24: 2797. Available from: doi: 10.3390/molecules24152797.
[34] Ahmad T, Ansari MZ. Enhancement of infrared shielding property of SnO_2 using Sb as a dopant. *Materials Research Express*. 2022; 9: 105902. Available from: doi: 10.1088/2053-1591/ac9778.
[35] Guillén C, Herrero J. Structural and plasmonic characteristics of sputtered SnO_2:Sb and ZnO:Al thin films as a function of their thickness. *Journal of Materials Science*. 2016; 51: 7276-7285. Available from: doi: 10.1007/s10853-016-0010-9.